Supplementary Material

FeCo bimetallic phosphides heterostructure for hydrogen production via sulfion oxidation assisted alkaline seawater splitting

Junyang Ding[a,b]†, Hao Wang[e]†, Guolong Lu[c], Liuyu Ji[c], Hengwen Li[c], Peipei Jia[b], Chengjie Li[d], Xijun Liu[c]*, and Jun Luo[b]**

[a] *University of Electronic Science and Technology of China, Chengdu 611731, China*

[b] *ShenSi Lab, Shenzhen Institute for Advanced Study, University of Electronic Science and Technology of China, Longhua District, Shenzhen 518110, China*

[c] *Guangxi Key Laboratory of Processing for Non-ferrous Metals and Featured Materials, MOE Key Laboratory of New Processing Technology for Nonferrous Metals and Materials, School of Resources, Environment and Materials, Guangxi University, Nanning 530004, Guangxi, China*

[d] *School of Material Science and Engineering, Sun Yat-Sen University, Guangzhou 510006, China*

[e] *Oil & Gas Technology Research Institute of Qinghai Oilfield Company, CNPC, Jinda East Road, Qili Town, Dunhuang, Jiuquan, Gansu 736202, China*

Authors to whom correspondence should be addressed: jiapeipei@uestc.edu.cn, xjliu@gxu.edu.cn, jluo@uestc.edu.cn

† These authors contributed equally.

Experimental Section

Materials

Pure Al, Fe, and Co (purity, 99.9 %) are sourced from are sourced from ZhongNuo Advanced Material (Beijing) Technology Co., Ltd. Sodium sulfide nonahydrate ($Na_2S·9H_2O$, ≥98.0 %) and sublimed sulfur (CP grade) are taken from Macklin and Kermel, respectively. Potassium hydroxide (KOH, GR), hydrogen peroxide solution (H_2O_2, AR, 30 wt.% in H_2O), and sulfuric acid (H_2SO_4, 95.0~98.0%) are purchased from Sinopharm Chemical Reagent Co., Ltd. Natural seawater is obtained from the Yellow Sea, China. Platinum on carbon (PtC, 20 wt.%) and Nafion solution (5 wt.%) are from Hesen. Ruthenium(IV) oxide (RuO_2, ≥98.0 %) and Ethanol (C_2H_5OH, ≥99.7 %) are purchased from Aladdin. Distilled water with a resistivity higher than 18 MΩ·cm was used throughout the experiments.

Characterizations

X-ray diffraction (XRD) measurements were performed in the 2θ range of 10~80° on a Bruker D8 diffractometer operated at 40 kV and 40 mA with Cu Kα radiation to identify the crystalline phases. The surface morphology was characterized by scanning electron microscopy (SEM, FEI Quanta FEG 250) and transmission electron microscopy (TEM, FEI Talos F200X). Elemental distribution in selected regions was examined using a TEM equipped with energy-dispersive X-ray (EDX) for elemental mapping. The surface composition and chemical states were investigated by X-ray photoelectron spectroscopy (XPS) on a Thermo Fisher Scientific ESCALAB 250Xi system employing Al Kα radiation, and all binding energies were calibrated against the C 1s peak at 284.8 eV.

Electrochemical tests

The electrochemical measurements for HER/OER (1 M KOH + natural seawater) and SOR (1 M KOH + 1 M Na_2S + natural seawater) were performed on a CHI 760E electrochemical

workstation employing a conventional three-electrode configuration. A graphite rod (6.0 mm diameter) served as the counter electrode, while a Hg/HgO electrode (in 1 M KOH) was used as the reference electrode. The prepared powder samples (np-Fe_{10}-P, np-$Fe_{2.5}$Co-P, np-Fe_5Co-P, np-$Fe_{7.5}$Co-P, and np-Co_{10}-P) together with commercially available catalysts (20 wt.% Pt/C and RuO_2) were employed to fabricate the corresponding working electrodes. Specifically, a catalyst ink was prepared by dispersing 5 mg of catalyst powder in a mixed solution of 450 μL ethanol and 50 μL of 5 wt.% Nafion, followed by ultrasonication for 60 min in an ice-water bath to ensure uniform dispersion. For HER and OER, 100 μL of the dispersion was drop-coated onto a hydrophilic carbon paper conductive substrate (HCP020N, 1.0 ×2.0 cm^2; working area: 1.0 ×1.0 cm^2). For SOR, 100 μL was drop-coated onto a clean nickel foam (NF) conductive substrate (2 mm thick; 110 ppi pore size; 1.0 ×2.0 cm^2; working area: 1.0 ×1.0 cm^2), owing to the porous nature of NF, which facilitates the timely desorption of sulphur products. Catalyst-coated substrates were finally dried under an infrared lamp for 30 min prior to reserve. All measured potentials were converted to the reversible hydrogen electrode (RHE) scale according to the Nernst equation ($E_{RHE} = E_{Hg/HgO} + 0.059 \times pH + 0.098$ V), and 90% iR compensation was applied. Linear sweep voltammetry (LSV) was conducted at a scan rate of 5 mV s^{-1}. Electrochemical impedance spectroscopy (EIS) measurements were performed over a frequency range of 0.1 Hz to 100 kHz with an amplitude of 5 mV at an overpotential of 100 mV. The double-layer capacitance (C_{dl}) was determined from cyclic voltammetry (CV) curves collected within the non-Faradaic potential region to estimate the electrochemically active surface area (ECSA). Long-term stability was evaluated by chronoamperometry (CP) at a constant current density of 50 mA cm^{-2}. For the integrated HER||SOR configuration, a gas-tight H-type electrolytic cell equipped with a cation-exchange membrane (Nafion 117) was employed to separate the cathodic and anodic compartments.

Collection of sulfur product

Upon completion of the SOR process, the electrolyte pH was carefully adjusted to 1 by slowly adding 5 M H_2SO_4 under ice-bath conditions. After being left undisturbed overnight, a yellow precipitate formed at the bottom of the container. The solid product was collected, thoroughly washed with deionized water, separated via centrifugation, and subsequently dried at 60 °C for 24 h to yield yellow sulfur powder. [1]

TOF measurements

The turnover frequency (TOF) values were calculated according to the previously reported equation [2]:

$$TOF = j / (n \times F \times N)$$

Where j is the current density; n is the electron transfer number; and F is the Faraday constant (96485 C mol^{-1}).

The N values were the number of active centers measured by a widely used method [3]: Cyclic voltammetry (CV) measurements were performed when the scan rate was fixed at 50 mV s^{-1}. After this, by integrating the charge of the CV curve over the whole potential range, the half value of the charge was obtained, which is the value of the surface charge density (Q_S). Then, the N value was calculated using the following equation:

$$N = Q_S / F$$

where F is the Faraday constant (96485 C mol^{-1}).

DFT calculation

The computational model was constructed under the density functional theory (DFT) in the $Dmol^3$ code. The lattice structure was set to periodic 2x2 unit cells, i.e., each structure has four layers of metal atoms including the fixed two–layer bottom atom as well as other relaxed two–layer atoms for adsorbing objects. To analyze the Perdew–Burke–Emzerhof (PBE) exchange effect and related influence under the condition of generalized gradient

approximation, the vacuum space was set to 15 Å. And, the Brillouin zone was sampled with 3 × 3 × 1, the real space global orbit truncation radius is set to 4.5 Å. Nuclear processes and atomic charges were analyzed using the effective core potential (ECP) and Hirshfeld method, respectively.

The free energy of atomic structure is determined as follows:

$$\triangle G = \triangle E + \triangle ZPVE + \int C_P dT - T \triangle S$$

Where △E is the change of adsorption energy, △ZPVE is the difference of zero–point energy, and △S is the difference of entropy, C_p is the heat capacity, and T is the system temperature.

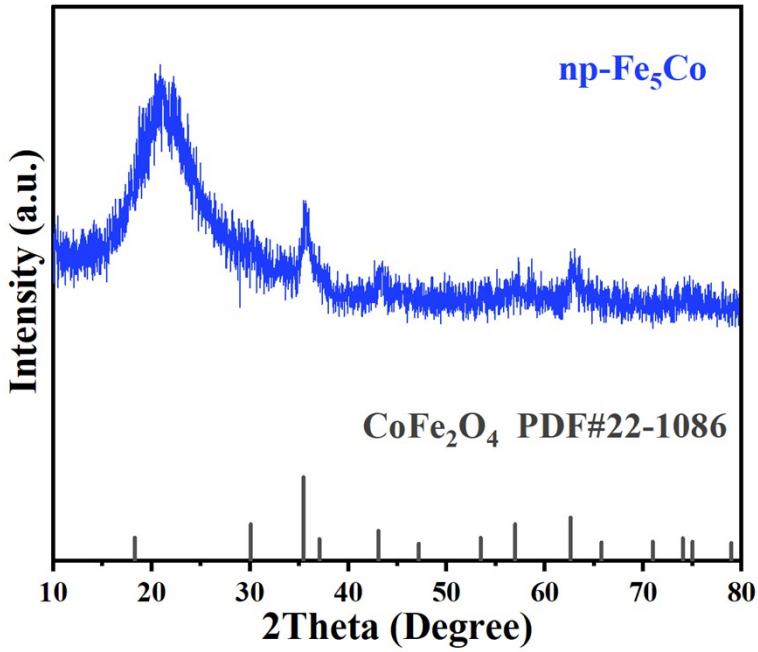

Figure S1. XRD pattern of np-Fe_5Co.

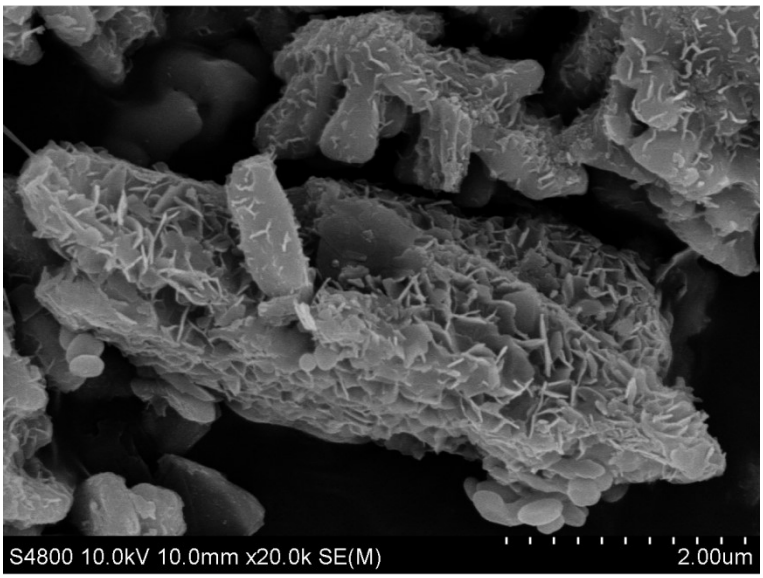

Figure S2. SEM image of np-Fe_5Co.

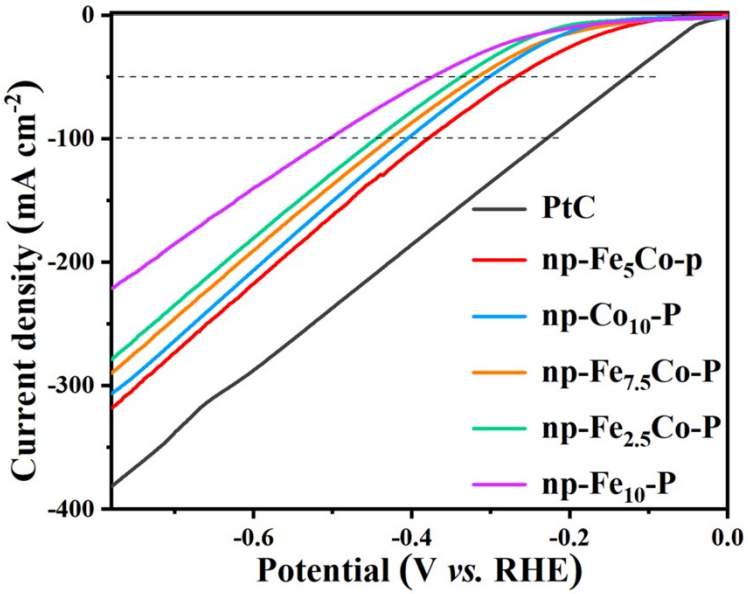

Figure S3. HER LSV curves of PtC, np-Fe_5Co-P, np-Co_{10}-P, np-$Fe_{7.5}$Co-P, np-$Fe_{2.5}$Co-P, and np-Fe_{10}-P without iR compensation.

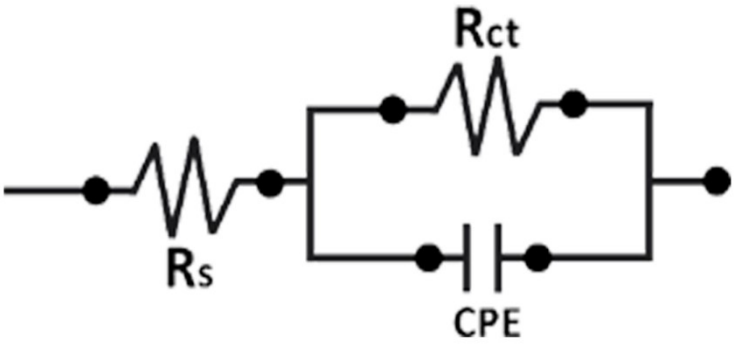

Figure S4. Equivalent electrical circuit (R_s is the solution resistance, R_{ct} is the charge transfer resistance, CPE is the constant phase element).

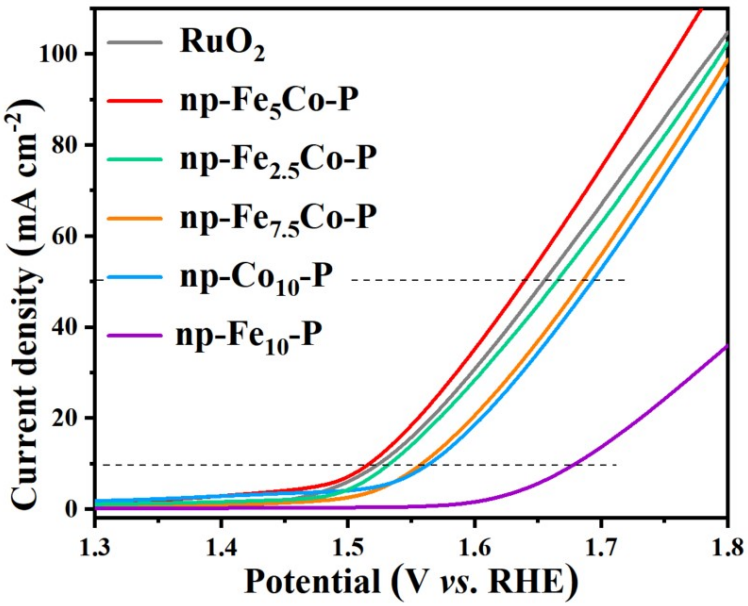

Figure S5. OER LSV curves of RuO_2, np-Fe_5Co-P, np-Co_{10}-P, np-$Fe_{7.5}$Co-P, np-$Fe_{2.5}$Co-P, and np-Fe_{10}-P without iR compensation.

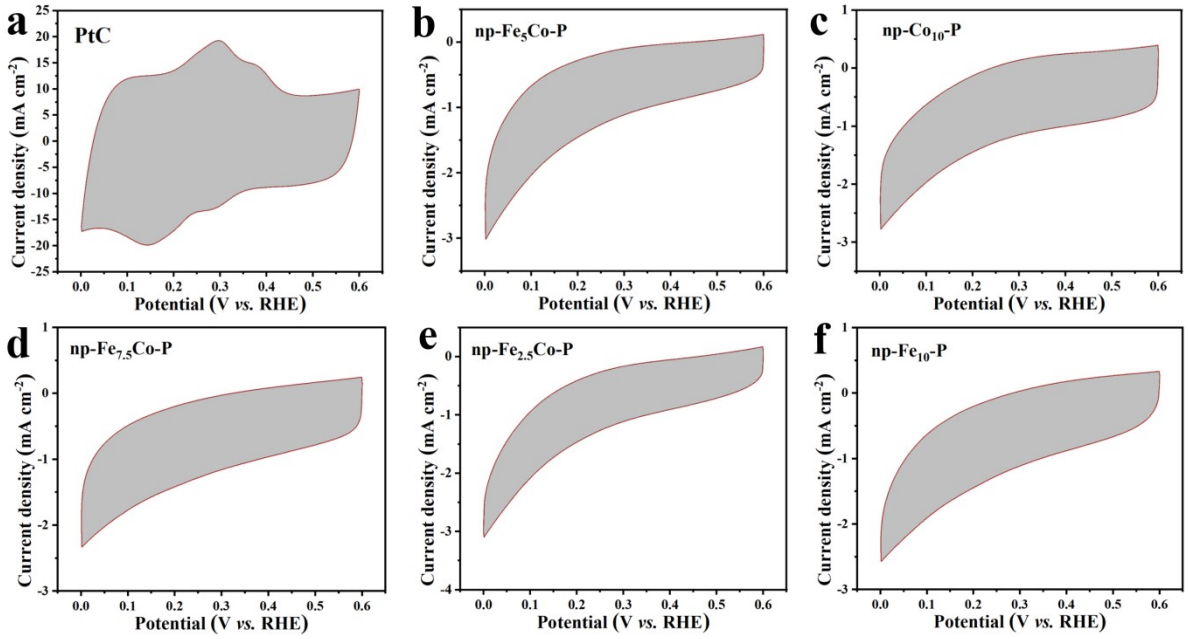

Figure S6. CV curves at 50 mV s^{-1} for PtC, np-Fe_5Co-P, np-Co_{10}-P, np-$Fe_{7.5}$Co-P, np-$Fe_{2.5}$Co-P, and np-Fe_{10}-P.

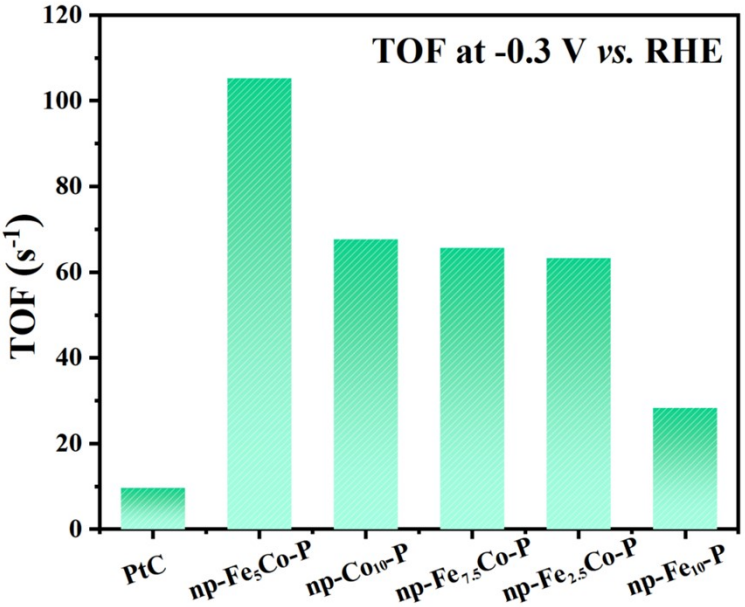

Figure S7. The calculated HER TOF values for PtC, np-Fe_5Co-P, np-Co_{10}-P, np-$Fe_{7.5}$Co-P, np-$Fe_{2.5}$Co-P, and np-Fe_{10}-P.

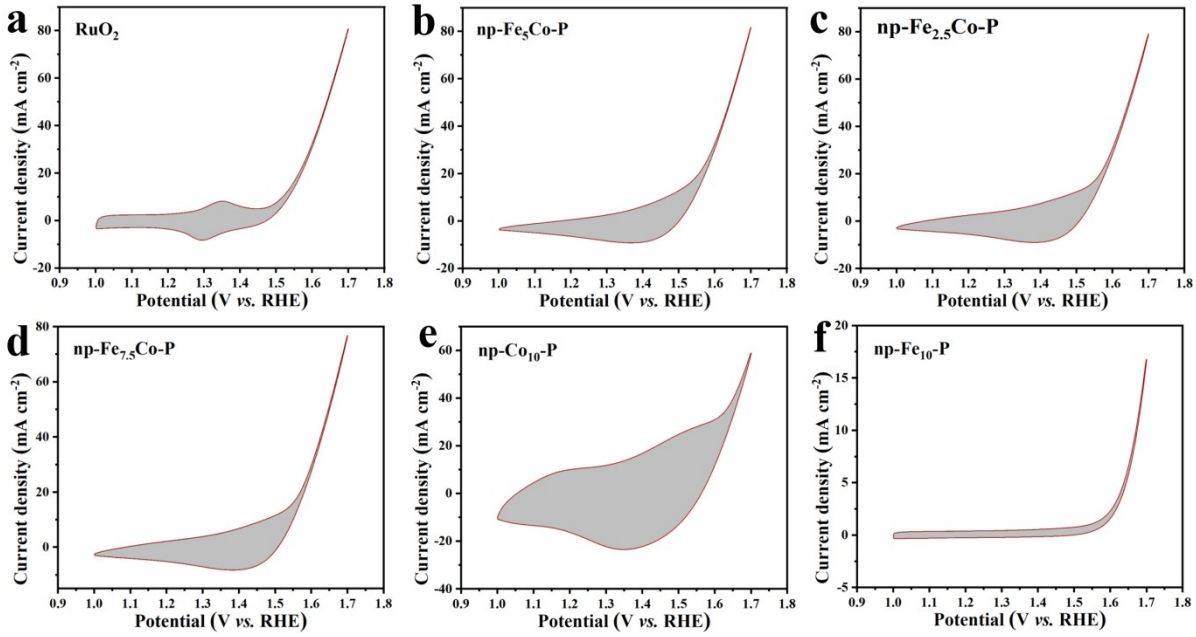

Figure S8. CV curves at 50 mV s^{-1} for RuO_2, np-Fe_5Co-P, np-Co_{10}-P, np-$Fe_{7.5}$Co-P, np-$Fe_{2.5}$Co-P, and np-Fe_{10}-P.

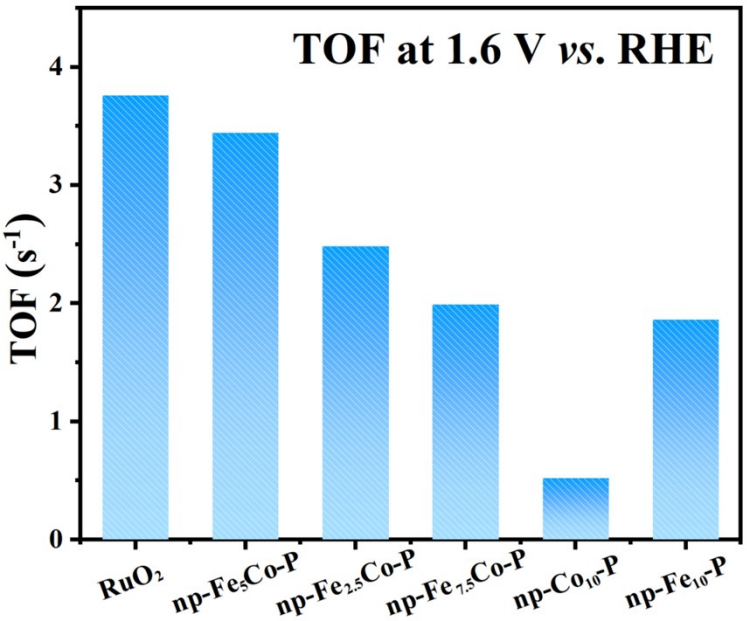

Figure S9. The calculated OER TOF values for RuO_2, np-Fe_5Co-P, np-Co_{10}-P, np-$Fe_{7.5}$Co-P, np-$Fe_{2.5}$Co-P, and np-Fe_{10}-P.

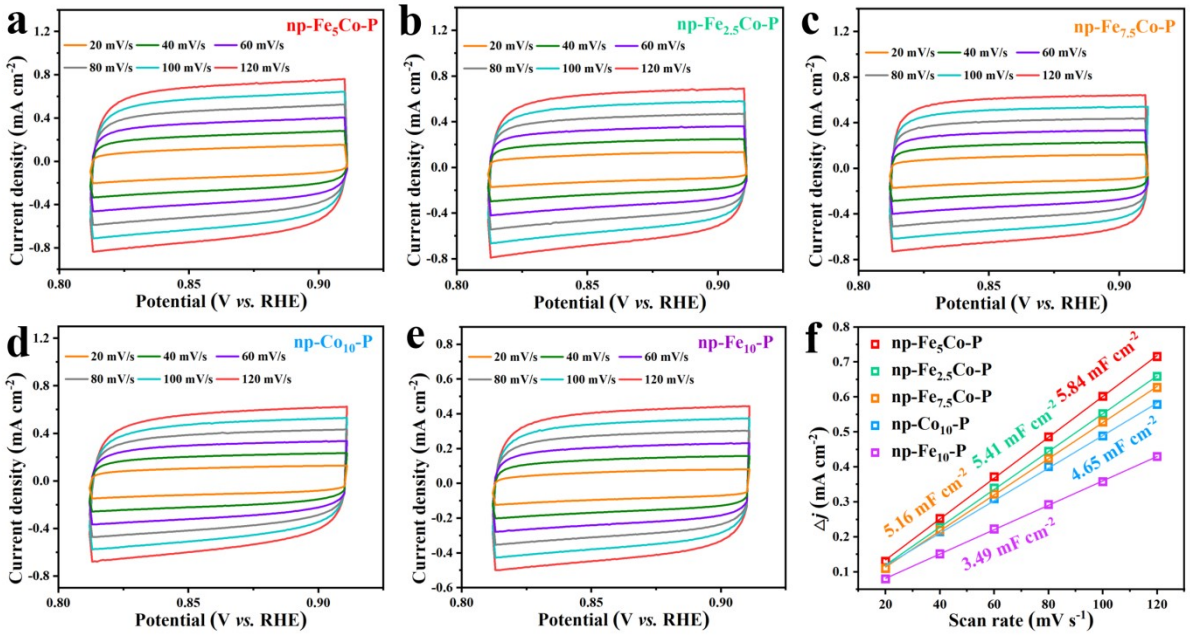

Figure S10. The CV curves at different scanning rates from 20 to 120 mV s^{-1} for (a) np-Fe_5Co-P, (b) np-$Fe_{2.5}$Co-P, (c) np-$Fe_{7.5}$Co-P, (d) np-Co_{10}-P, and (e) np-Fe_{10}-P. (f) The C_{dl} estimated from the scanning rate dependent CV curves.

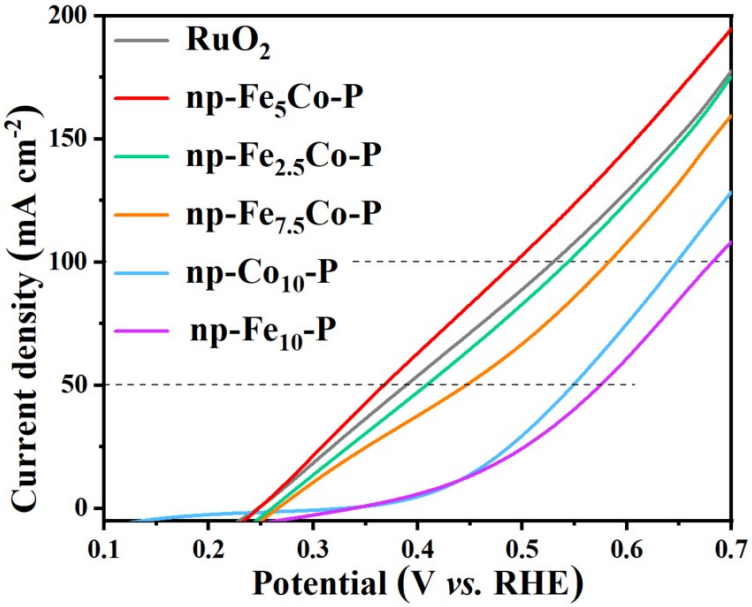

Figure S11. SOR LSV curves of RuO_2, np-Fe_5Co-P, np-Co_{10}-P, np-$Fe_{7.5}$Co-P, np-$Fe_{2.5}$Co-P, and np-Fe_{10}-P without iR compensation.

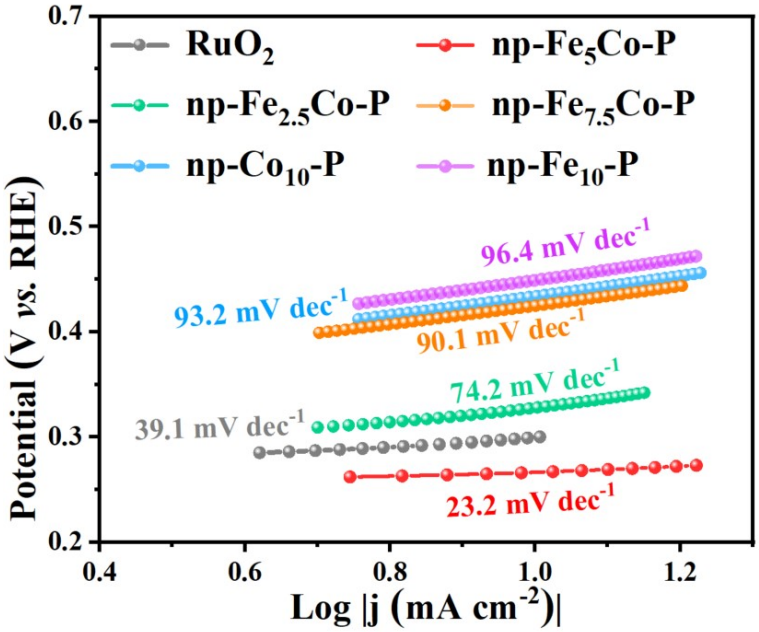

Figure S12. SOR Tafel plots of RuO_2, np-Fe_5Co-P, np-Co_{10}-P, np-$Fe_{7.5}$Co-P, np-$Fe_{2.5}$Co-P, and np-Fe_{10}-P.

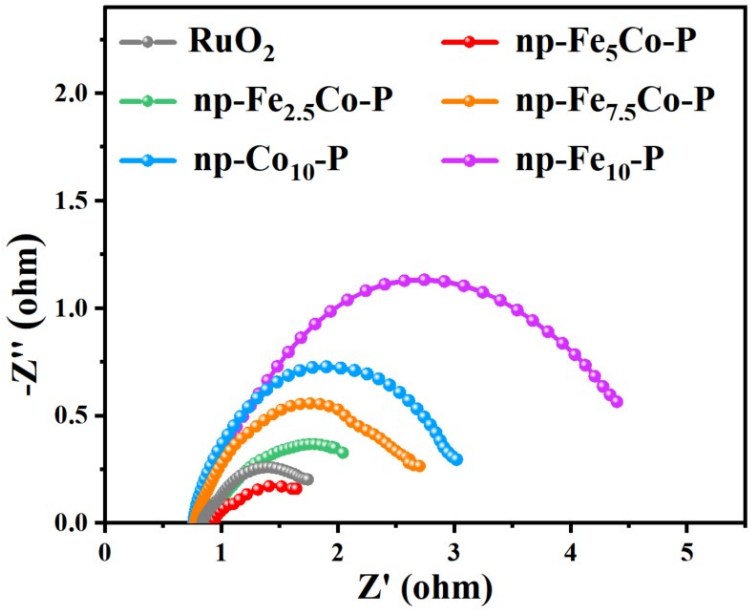

Figure S13. SOR Nyquist plots of RuO_2, np-Fe_5Co-P, np-Co_{10}-P, np-$Fe_{7.5}$Co-P, np-$Fe_{2.5}$Co-P, and np-Fe_{10}-P.

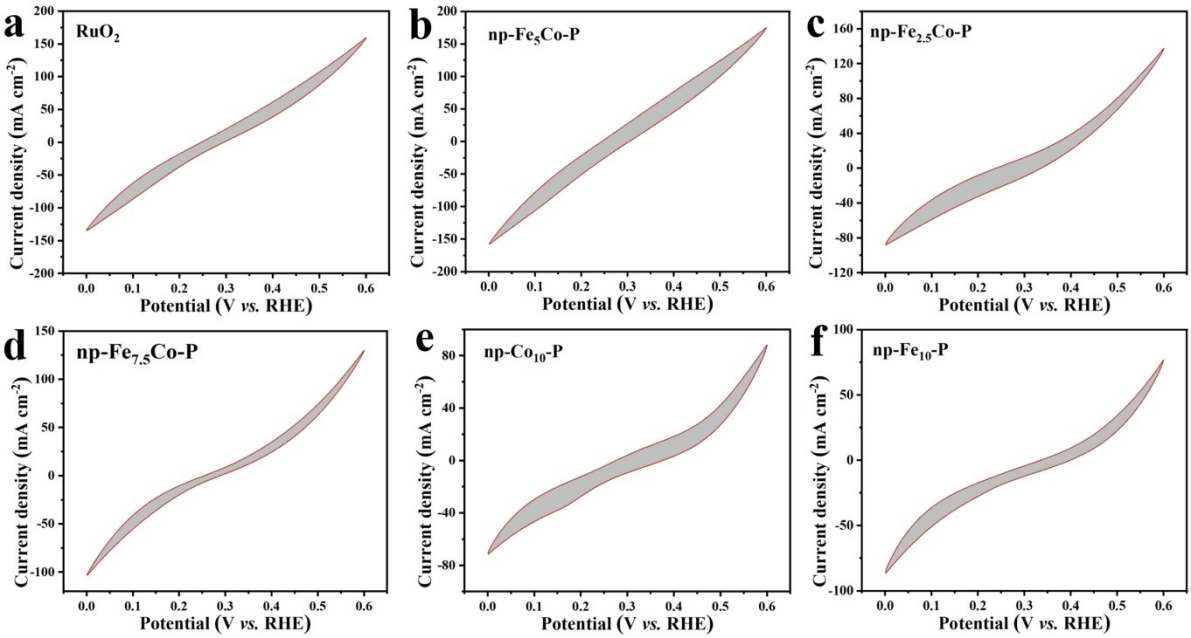

Figure S14. CV curves at 50 mV s^{-1} for RuO_2, np-Fe_5Co-P, np-Co_{10}-P, np-$Fe_{7.5}$Co-P, np-$Fe_{2.5}$Co-P, and np-Fe_{10}-P.

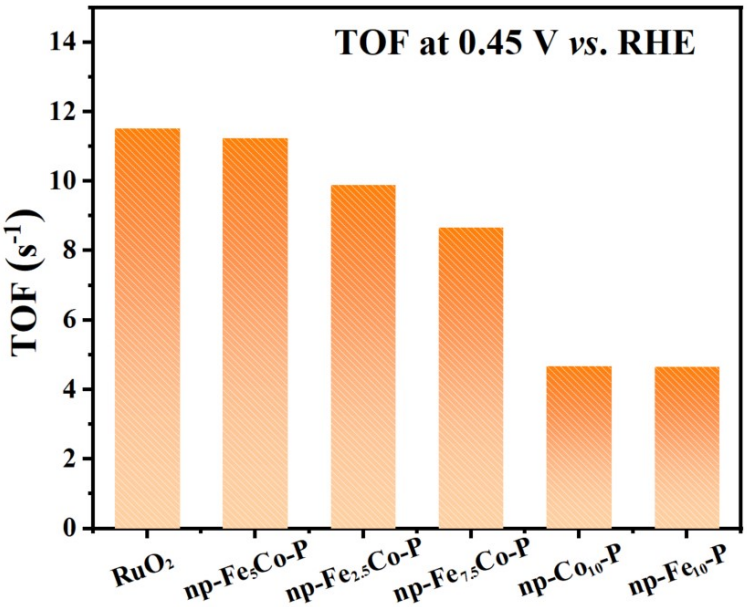

Figure S15. The calculated SOR TOF values for RuO_2, np-Fe_5Co-P, np-Co_{10}-P, np-$Fe_{7.5}$Co-P, np-$Fe_{2.5}$Co-P, and np-Fe_{10}-P.

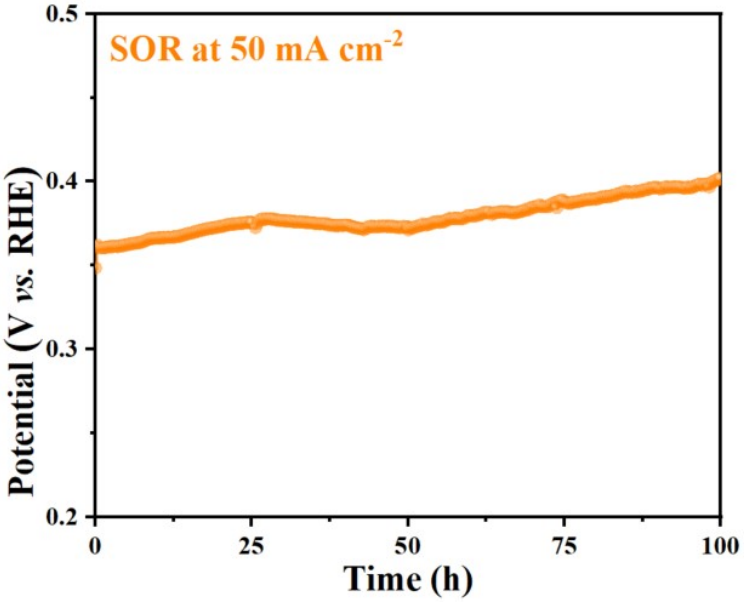

Figure S16. SOR CP stability test of np-Fe_5Co-P.

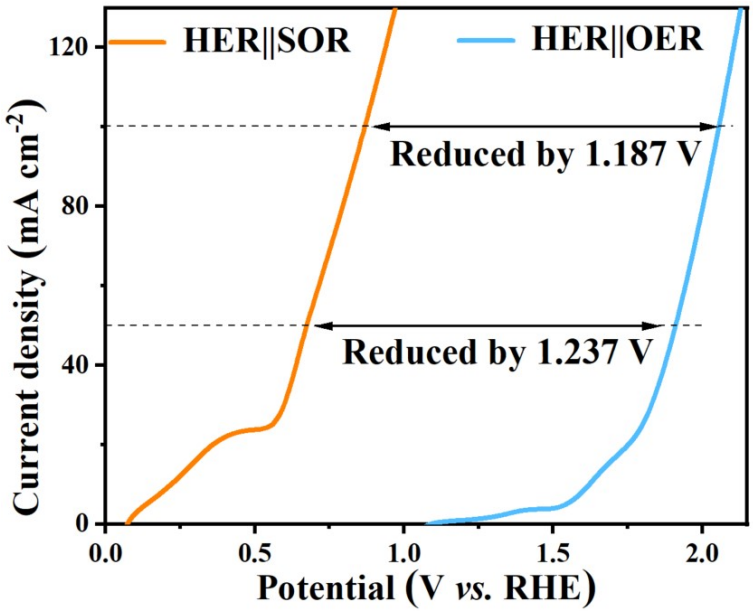

Figure S17. Comparison of LSV curves without iR compensation between HER||SOR with HER||OER seawater splitting systems.

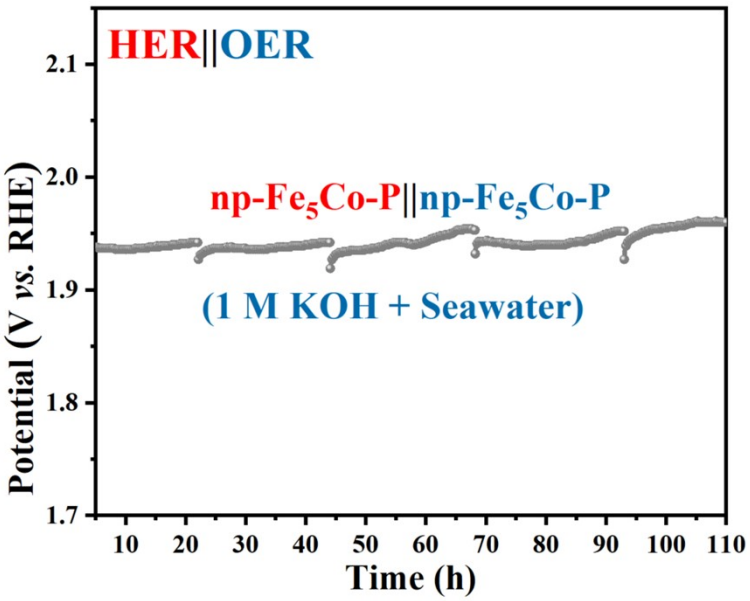

Figure S18. CP stability test of HER||OER seawater splitting systems.

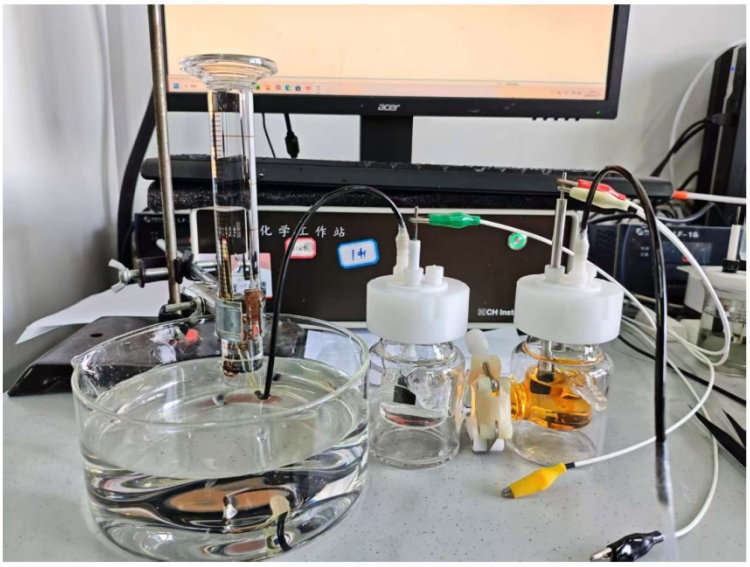

Figure S19. Devices for measuring Faraday efficiency of H_2 product in the HER||SOR alkaline seawater splitting system.

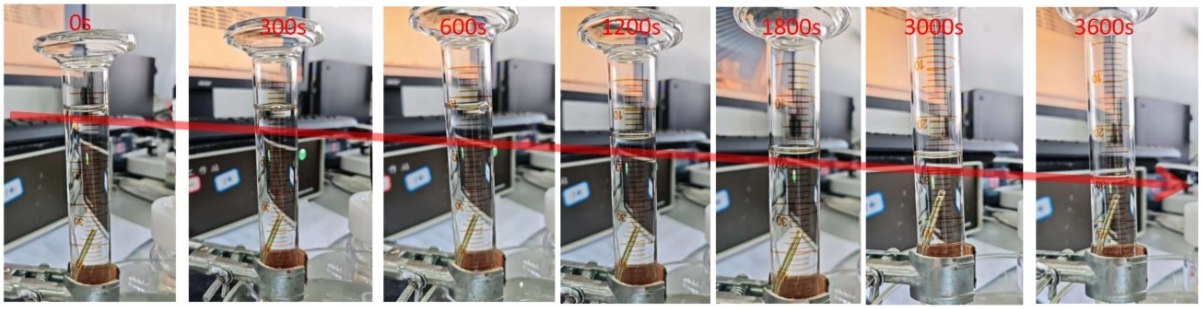

Figure S20. Photo of the change in hydrogen gas volume over time in a HER||SOR coupled electrolysis system.

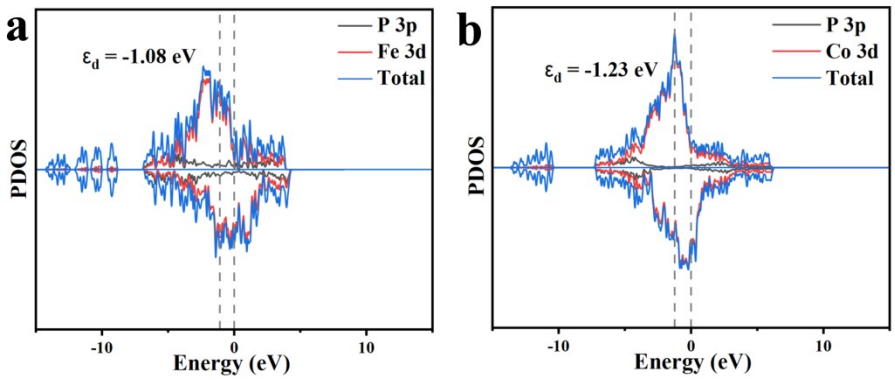

Figure S21. The calculated DOS results of FeP and Co_2P.

Table S1 Comparison of R_{ct} values obtained from equivalent electrical circuit of np-Fe_5Co-P and control samples in alkaline seawater electrolytes for HER.

Catalyst	R_s (Ω)	R_{ct} (Ω)	CPE-T	CPE-P
PtC	1.71	0.35	1.77×10^{-1}	7.63×10^{-1}
np-Fe_5Co-P	1.84	1.76	3.99×10^{-2}	8.05×10^{-1}
np-Co_{10}-p	1.83	3.48	1.69×10^{-2}	8.64×10^{-1}
np-$Fe_{7.5}$Co-P	1.77	4.35	1.16×10^{-2}	8.55×10^{-1}
np-$Fe_{2.5}$Co-P	1.83	6.38	1.88×10^{-2}	8.61×10^{-1}
np-Fe_{10}-P	1.97	11.12	1.01×10^{-1}	5.06×10^{-1}

R_s is solution resistance, R_{ct} is charge transfer resistance, CPE is constant phase element.

Table S2 Comparison of R_{ct} values obtained from equivalent electrical circuit of np-Fe_5Co-P and control samples in alkaline seawater electrolytes for OER.

Catalyst	R_s (Ω)	R_{ct} (Ω)	CPE-T	CPE-P
RuO_2	1.63	2.51	5.80×10^{-2}	8.17×10^{-1}
np-Fe_5Co-P	1.77	1.62	2.23×10^{-2}	7.94×10^{-1}
np-$Fe_{2.5}$Co-P	2.10	2.70	9.16×10^{-2}	7.83×10^{-1}
np-$Fe_{7.5}$Co-P	1.83	5.10	2.66×10^{-2}	7.73×10^{-1}
np-Co_{10}-P	1.99	5.27	4.18×10^{-3}	8.38×10^{-1}
np-Fe_{10}-P	2.13	8.10	4.12×10^{-2}	8.83×10^{-1}

R_s is solution resistance, R_{ct} is charge transfer resistance, CPE is constant phase element.

Table S3 Comparison of R_{ct} values obtained from equivalent electrical circuit of np-Fe_5Co-P and control samples in S^{2-}-consisting alkaline seawater electrolytes for SOR.

Catalyst	R_s (Ω)	R_{ct} (Ω)	CPE-T	CPE-P
RuO_2	0.83	1.14	1.56×10^{-1}	5.63×10^{-1}
np-Fe_5Co-P	0.90	1.06	2.94×10^{-1}	4.10×10^{-1}
np-$Fe_{2.5}$Co-P	0.89	1.56	3.35×10^{-1}	5.64×10^{-1}
np-$Fe_{7.5}$Co-P	0.76	2.02	2.13×10^{-2}	6.52×10^{-1}
np-Co_{10}-P	0.77	2.40	4.37×10^{-3}	7.15×10^{-1}
np-Fe_{10}-P	0.78	4.13	2.05×10^{-2}	6.50×10^{-1}

R_s is solution resistance, R_{ct} is charge transfer resistance, CPE is constant phase element.

Table S4 Comparison of the HER||SOR coupled electrolytic system assembled using the np-Fe_5Co-P catalyst developed in this study with other recently reported works.

Catalyst	Cathode Electrolyte	Anode Electrolyte	Potential@ Current Density (V@mA cm^{-2})	Stability (mA cm^{-2}@h)	Reference
np-Fe_5Co-P	1 M KOH + seawater	1 M KOH + 1 M Na_2S + seawater	0.636@50 0.759@100	50@300	This work
$Ni(OH)_2/NiS_x$/ NF-350	1 M KOH + seawater	1 M KOH + 1 M Na_2S + seawater	0.843@100	50@36	Mater. Chem. Front., 2025, 9, 2658-2667.
NiCo-S/NiCo-OH-CL	1 M NaOH	1 M NaOH + 2M Na_2S	0.62@100	100@3200	Energy Environ. Mater., 2026, e70261.
$NiFeC_2O_4$–S	1 M NaOH	1 M NaOH + 1M Na_2S	0.542@100	200@100	Chem. Commun., 2026, 62, 594-598.
Co-SAs-PNC	2 M Na_2S + seawater	2 M Na_2S + seawater	1.01@500	500@450	Adv. Funct. Mater., 2026, e25588
Pd_3S NTs	1 M KOH	1 M KOH + 4 M Na_2S	0.449@10	10@120	Fuel, 2026, 408, 137613.
MoS_2/Co_8FeS_8 /Ni_3S_2/NF	1 M KOH + 1 M Na_2S	1 M KOH + 1 M Na_2S	0.082@10 0.293@50	200@200	Adv. Funct. Mater., 2026, 36, e19053.
NiTe@NiMo/ NFNi–P/NF	1 M NaOH + 0.5 M NaCl	1 M NaOH + 0.5 M NaCl + 1 M Na_2S	0.496@100	1000@190	Energy Environ. Sci., 2025, 18, 1440-1451

Reference

[1] Adv. Funct. Mater., 2023, 33, 2212183.

[2] Nat. Commun., 2018, 9, 4365.

[3] Int. J. Hydrogen Energy, 2024, 90, 747-756.